

## PAPER



Cite this: *Phys. Chem. Chem. Phys.*,  
2020, 22, 23657

# Kinetic study of the $\text{OH} + \text{HO}_2 \rightarrow \text{H}_2\text{O} + \text{O}_2$ reaction using ring polymer molecular dynamics and quantum dynamics†

Yang Liu, <sup>a</sup> Hongwei Song <sup>\*b</sup> and Jun Li <sup>\*a</sup>

The reaction  $\text{OH} + \text{HO}_2 \rightarrow \text{H}_2\text{O} + \text{O}_2$  is a prototype of radical–radical reactions. It plays an important role in interstellar/atmospheric chemistry and combustion, and considerable attention has thus been dedicated to its kinetics. In our previous work, we reported an accurate full-dimensional potential energy surface for the title reaction on the ground triplet electronic state. The quasi-classical trajectory (QCT) approach was employed to investigate its kinetics. Although the QCT rate coefficients were in good agreement with some experimental and theoretical results, QCT cannot account for the quantum mechanical effects, such as zero-point vibrational energy, recrossing, and tunneling, which may significantly affect the rate coefficients, particularly at low temperatures. In this work, the reduced-dimensional quantum dynamics and ring polymer molecular dynamics calculations were carried out to examine these effects and their impact on rate coefficients over the temperature range of 300–1300 K.

Received 4th August 2020,  
Accepted 25th September 2020

DOI: 10.1039/d0cp04120c

rsc.li/pccp

## 1. Introduction

The reaction  $\text{OH} + \text{HO}_2 \rightarrow \text{H}_2\text{O} + \text{O}_2$  (R1) has attracted considerable attention due to its significance in atmospheric chemistry and combustion, as well as the interstellar medium. In the upper atmosphere, on the one hand, R1 is a major step in the removal of OH and  $\text{HO}_2$ , both of which are related to other important atmospheric species including O,  $\text{O}_3$ ,  $\text{ClO}_x$ , and  $\text{NO}_x$ .<sup>1</sup> On the other hand, R1 is the main termination process for the  $\text{HO}_2$  radical in lean combustion and is thus responsible for the depletion of both radicals in burnt gases.<sup>2–5</sup> The thermal rate coefficients of R1 ( $k_{\text{R1}}$ ) show an anomalous temperature dependence, *i.e.*, the striking negative temperature dependence at low temperatures, and the mildly positive dependence at high temperatures, which serve as an ideal ground proving for testing different rate theories. The accurate measurement of  $k_{\text{R1}}$  is difficult due to the following factors: the radical–radical nature of the reaction, the difficulty of monitoring the radical concentrations (especially  $\text{HO}_2$ ), and the virtually unavoidable side- and self-reactions.<sup>6</sup> Facing these long-standing difficulties, many experimentalists have dedicated

themselves to accurately measuring its rate coefficients but these measurements are quite scattered in the entire temperature range.<sup>1–3,5–28</sup> Therefore, R1 has been considered as “the Holy Grail Reaction” by Fred Kaufman.<sup>24</sup>

Theoretically, Mozurkewich calculated  $k_{\text{R1}}$  at 298 K using the Rice–Ramsperger–Kassel–Marcus (RRKM) theory and found a negative temperature dependence over the 250–420 K range.<sup>29</sup> Toohey and Anderson used the Møller–Plesset perturbation theory to compute a classical barrier height of 2.5 kcal mol<sup>−1</sup> on the triplet electronic state. They attributed the large  $k_{\text{R1}}$  to the long-range dipole–dipole attraction between reactants, which facilitates the formation of a hydrogen-bonded complex.<sup>30</sup> Gonzalez *et al.* computed  $k_{\text{R1}}$  on both singlet and triplet potential energy surfaces (PESs) and concluded that  $k_{\text{R1}}$  on the singlet PES is negligible due to its higher barrier.<sup>31,32</sup> The reported rate coefficients showed a slightly negative temperature dependence over 200–2000 K.<sup>32</sup> In 2013, a multi-scale modeling approach was employed by Burke *et al.* to investigate the apparent anomalous temperature dependence of  $k_{\text{R1}}$ , which was well represented by the following bi-Arrhenius expression over 200–3000 K:  $k_{\text{R1}} = 3.21 \times 10^{-4} T^{-2.49} \exp[-294/T] + 2.01 \times 10^{-15} T^{1.24} \exp[658/T]$  cm<sup>3</sup> molecule<sup>−1</sup> s<sup>−1</sup> with a minimum at 1200 K.<sup>33</sup> Zhang *et al.* calculated  $k_{\text{R1}}$  using the conventional transition state theory (TST) with the electronic information determined at the level of CCSD(T)/aug-cc-pVTZ//CCSD/6-311G(d,p). The obtained  $k_{\text{R1}}$  varied from  $2.30 \times 10^{-11}$  to  $2.37 \times 10^{-11}$  cm<sup>3</sup> molecule<sup>−1</sup> s<sup>−1</sup> in the range of 216.2–298.2 K.<sup>34</sup> Later, Zhang *et al.* re-investigated the kinetics of R1 at the CCSD(T)/aug-cc-pVTZ//M06-2X/aug-cc-pVTZ level, and modified  $k_{\text{R1}}$  to be  $2.24\text{--}8.62 \times 10^{-11}$  cm<sup>3</sup> molecule<sup>−1</sup> s<sup>−1</sup> over the

<sup>a</sup> School of Chemistry and Chemical Engineering & Chongqing Key Laboratory of Theoretical and Computational Chemistry, Chongqing University, Chongqing 401331, China. E-mail: jli15@cqu.edu.cn

<sup>b</sup> State Key Laboratory of Magnetic Resonance and Atomic and Molecular Physics, Wuhan Institute of Physics and Mathematics, Innovation Academy for Precision Measurement Science and Technology, Chinese Academy of Sciences, Wuhan 430071, China. E-mail: hwsong@wipm.ac.cn

† Electronic supplementary information (ESI) available. See DOI: 10.1039/d0cp04120c

temperature range of 240–425 K.<sup>35</sup> Using microcanonical and multi-structural canonical TSTs, Monge-Palacios and Sarathy found that the rate coefficients on the triplet and singlet PESs in the temperature range of 200–2500 K can be represented by  $k_{R1} = 5.12 \times 10^{-12} T^{0.07} \exp[1151/RT] + 1.33 \times 10^{-11} T^{0.32} \exp[-6896/RT] \text{ cm}^3 \text{ molecule}^{-1} \text{ s}^{-1}$  and  $k_{R1} = 3.55 \times 10^{-18} T^{1.65} \exp[-2180/RT] \text{ cm}^3 \text{ molecule}^{-1} \text{ s}^{-1}$ , respectively. They concluded that the branching ratio of R1 on the singlet PES is less than 0.5% below 1000 K, *i.e.*, the reaction primarily takes place on the triplet PES.<sup>36</sup> In 2020, the Gaussian process regression (GPR) method<sup>37,38</sup> was implemented by Song *et al.*<sup>39</sup> to fit a full-dimensional PES based on  $\sim 4600$  *ab initio* points at the level of CCSD(T)-F12a/aug-cc-pVTZ. They computed  $k_{R1}$  using the ring polymer molecular dynamics (RPMD)<sup>40</sup> method at the temperatures of 300, 400, 500 and 1000 K on this GPR PES, which has a fitting error of  $\sim 21$  meV. The GPR approach has demonstrated its prowess in approaching convergence based on much fewer data points as compared to other fitting methods.<sup>37,38</sup> Besides, the GPR approach can avoid overfitting,<sup>38</sup> and provide a guide for adding new data points.<sup>38,41</sup> However, the scaling of the calculation cost is poor in both training and evaluation for GPR PESs.

In our previous work, we constructed an accurate triplet state full-dimensional PES<sup>42</sup> based on  $\sim 108\,000$  CCSD(T)-F12a/aug-cc-pVTZ data points using the permutation invariant polynomial-neural network (PIP-NN) method.<sup>43–45</sup> The fitting root mean squared error was 12.6 meV, thanks to the high-fidelity PIP-NN fitting method with exact permutation symmetry. Quasi-classical trajectory (QCT) calculations were performed to compute  $k_{R1}$  at the temperatures of 100, 200, 300, 500, 1000, 1500, 2000 and 3000 K. Recently, we further studied the dynamics of the title reaction using QCT and reduced-dimensional quantum dynamical (QD) approaches on this global full-dimensional PES. Surprisingly, it was found that the vibrational excitation of the spectator OH bond significantly enhanced the reactivity at low collision energies due to the increased dipole of the vibrationally excited OH, which increased the chance of capturing the reactants to form a transition-state-like hydrogen-bonded complex.

Since the QCT method cannot describe the quantum mechanical effects, the obtained rate coefficients need to be further inspected. Herein, both RPMD and QD approaches are employed to revisit  $k_{R1}$  on our previous PIP-NN PES.<sup>42</sup> The RPMD method is an approximate quantum mechanical approach with full dimensionality. It can efficiently and accurately describe the zero-point vibrational energy (ZPVE), recrossing, and tunneling effects. Furthermore, the rate coefficients calculated by RPMD are not affected by the choice of the transition state dividing surface,<sup>47</sup> which is highly valuable since it is hard to define the dividing surface in the multi-dimensional configuration space of polyatomic reactions. The RPMD theory has been proved to provide reliable thermal rate coefficients for many bimolecular reactions over wide temperature ranges, as compared to the results computed by the exact QD theory and available experimental measurements.<sup>47–51</sup> As shown in Fig. 1, the title reaction has a relatively deep reaction complex, RC, which is 5.87 kcal mol<sup>−1</sup> lower than the reactant asymptote; also, the barrier was only  $-1.45$  kcal mol<sup>−1</sup>. Therefore, the anomalous kinetics of the title reaction mentioned above

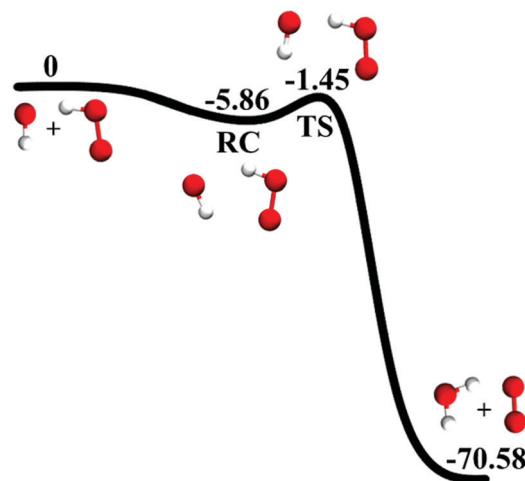


Fig. 1 Schematic reaction path for the title reaction on the PIP-NN PES. Energies are in kcal mol<sup>−1</sup> and relative to the reactant asymptote.

provides a unique test for the fascinating RPMD theory. The QD calculations, which inherently include quantum effects but are much more computationally demanding, were also carried out for comparison. The remainder of the present work is organized as follows. The RPMD and QD methodologies are described in Section II. The results and discussion are given in Section III. Finally, conclusions are summarized in Section IV.

## II. Theory

### II.A Quantum dynamical calculations

The initial state-selected time-dependent wave packet method has been detailed in the literature.<sup>52</sup> Here, we briefly outline the related aspects. The Hamiltonian in the reactant diatom-triatom Jacobi coordinates for a given total angular momentum  $J_{\text{tot}}$  can be written as follows ( $\hbar = 1$  hereafter):<sup>53</sup>

$$\hat{H} = -\frac{1}{2\mu_R} \frac{\partial^2}{\partial R^2} - \frac{1}{2\mu_{r_1}} \frac{\partial^2}{\partial r_1^2} - \frac{1}{2\mu_{r_2}} \frac{\partial^2}{\partial r_2^2} + \frac{(\hat{J}_{\text{tot}} - \hat{J})^2}{2\mu_R R^2} + \frac{\hat{J}_1^2}{2\mu_{r_1} r_1^2} + \frac{\hat{J}_2^2}{2\mu_{r_2} r_2^2} + \frac{\hat{J}_3^2}{2\mu_{r_3} r_3^2} + \hat{V}(R, r_1, r_2, \theta_1, \theta_2, \theta_3, \varphi_1, \varphi_2; r_{3e}), \quad (1)$$

where  $R$  is the distance between the centers of mass (COMs) of OH and HO<sub>2</sub>,  $r_1$  is the bond distance of the OH reactant,  $r_2$  denotes the distance from H in HO<sub>2</sub> to the COM of O<sub>2</sub> in HO<sub>2</sub> and  $r_3$  is the bond distance of the nonbroken O<sub>2</sub> bond.  $\theta_1, \theta_2, \theta_3$  are the angles formed by  $R$  and  $r_1$ ,  $R$  and  $r_2$ ,  $R$  and  $r_3$ , respectively.  $\varphi_1$  is the torsional angle between the planes ( $R, r_1$ ) and ( $R, r_2$ ).  $\varphi_2$  is the torsional angle between the planes ( $R, r_2$ ) and ( $r_2, r_3$ ).  $\mu_R, \mu_{r_1}, \mu_{r_2}$ , and  $\mu_{r_3}$  stand for the reduced masses of OH–HO<sub>2</sub>, OH, H–O<sub>2</sub>, and O<sub>2</sub>, respectively.  $\hat{J}_3$  is the rotational angular momentum operator of O<sub>2</sub> and  $\hat{J}_2$  is the orbital angular momentum operator of the atom H with respect to O<sub>2</sub> in HO<sub>2</sub>. The coupling of  $\hat{J}_3$  and  $\hat{J}_2$  gives rise to  $\hat{J}_{23}$ , which is the angular momentum operator of HO<sub>2</sub>. The coupling of  $\hat{J}_1$ ,

which is the rotational angular momentum operator of OH, with  $\hat{j}_{23}$  gives rise to  $\hat{j}$ . Since the reaction involves three heavy oxygen atoms,  $r_3$  is fixed at the equilibrium geometry of the reactant HO<sub>2</sub>,  $r_{3e} = 2.5105a_0$ , to reduce the computational cost. This treatment is thought to be solid, considering that the bond distance of O<sub>2</sub> varies slightly along the minimum energy path (MEP) near the TS region. The shortening of the O<sub>2</sub> bond in the product channel is considered to have a negligible effect on the total reaction probability due to the high exothermicity.

The time-dependent wave function of the system is expanded in terms of the body-fixed (BF) ro-vibrational basis functions as follows:

$$\begin{aligned} \psi^{J_{\text{tot}} M_E}(\vec{R}, \vec{r}_1, \vec{r}_2, \vec{r}_3) = & \sum_{n, \nu_1, \nu_2, j, K} C_{n\nu_1\nu_2JK}^{J_{\text{tot}} M_E}(t) u_n^{\nu_2}(R) \\ & \times \phi_{\nu_1}(r_1) \phi_{\nu_2}(r_2) \Phi_{JK}^{J_{\text{tot}} M_E}(\hat{R}, \hat{r}_1, \hat{r}_2, \hat{r}_3), \end{aligned} \quad (2)$$

where  $C_{n\nu_1\nu_2JK}^{J_{\text{tot}} M_E}$  are time-dependent expansion coefficients.  $n$  labels the translational basis functions,  $\nu_1$  and  $\nu_2$  are the vibrational basis indices, the composite index  $j$  denotes  $(j_1, l_2, j_3, j_{23}, J)$ . The translational basis function  $u_n^{\nu_2}(R)$ , defined as the sine function, depends on  $\nu_2$  due to the employment of an L-shaped grid.<sup>54</sup>

The initial wave packet  $|\chi_i\rangle$  was constructed by a direct product of a localized Gaussian wave packet along the scattering coordinate  $R$  and a specific  $(J_{\text{tot}} K_E)$  state of the reactive system, which is propagated from the reactant asymptote by the second-order split-operator method.<sup>55</sup> The centrifugal sudden approximation,<sup>56,57</sup> i.e., neglecting the coupling between different  $K$  blocks, was employed as well. To prevent artificial boundary reflections, the negative imaginary absorbing potential was applied at the edges of the grid.<sup>58</sup>

The total reaction probability from a specific initial state is determined according to the following equation:

$$P_{\text{vOH vHO}_2 \text{ jOH jHO}_2}^{J_{\text{tot}} E}(E_{\text{trans}}) = \langle \chi_i^+(E_{\text{trans}}) | \hat{F} | \chi_i^+(E_{\text{trans}}) \rangle, \quad (3)$$

where the flux operator is defined as  $\hat{F} = \text{Im} \left[ \frac{1}{\mu_{r_2}} \delta(r_2 - r_2^F) \frac{\partial}{\partial r_2} \right]$ .<sup>59</sup>

The energy-dependent scattering wavefunction,  $\psi_i^+(E)$ , is computed by Fourier transform of the time-dependent wave packet at the dividing surface  $S[r_2 = r_2^F]$ . The integral cross section (ICS) is calculated by summing the reaction probabilities from the specific initial state over all relevant partial waves:

$$\begin{aligned} \sigma_{\text{vOH vHO}_2 \text{ jOH jHO}_2}(E_{\text{trans}}) = & \frac{1}{(2j_{\text{OH}} + 1)(2j_{\text{HO}_2} + 1)} \sum_{JK} \frac{\pi}{k^2} \\ & \times \sum_{J_{\text{tot}} \geq K} (2J_{\text{tot}} + 1) P_{\text{vOH vHO}_2 \text{ jOH jHO}_2}^{J_{\text{tot}} E}(E_{\text{trans}}) \end{aligned} \quad (4)$$

where  $K$  is taken from 0 to  $\min(J, J_{\text{tot}})$ .

The initial state-specific rate constant is calculated by thermally averaging the collision energy of the corresponding

ICS as follows:

$$\begin{aligned} k_{\text{vOH vHO}_2 \text{ jOH jHO}_2}(T) = & \sqrt{\frac{8k_B T}{\pi \mu}} \frac{1}{(k_B T)^2} \int_0^\infty dE_{\text{trans}} E_{\text{trans}} \\ & \times \exp(-E_{\text{trans}}/k_B T) \times \sigma_{\text{vOH vHO}_2 \text{ jOH jHO}_2}(E_{\text{trans}}). \end{aligned} \quad (5)$$

In the QD calculations, the reactants OH and HO<sub>2</sub> were both restricted in ground ro-vibrational states due to the extremely expensive computational cost involved. The numerical parameters employed in this work are the same as in ref. 46.

## II.B Ring polymer molecular dynamical calculations

The RPMD rate code,<sup>60</sup> implemented by Suleimanov *et al.*, was employed to calculate the thermal rate coefficients of R1. The details of the RPMD methodology can be found in the literature.<sup>47,61</sup> Briefly, according to the Bennett–Chandler factorization,<sup>62</sup> the RPMD rate coefficient can be expressed as follows:<sup>63,64</sup>

$$k_{\text{RPMD}} = k_{\text{QTST}}(T; \xi^\ddagger) \kappa(t \rightarrow \infty; \xi^\ddagger). \quad (6)$$

The first term  $k_{\text{QTST}}(T; \xi^\ddagger)$ , the static contribution, is the quantum transition state theory (QTST)<sup>65–67</sup> rate coefficient.<sup>68,69</sup>  $k_{\text{QTST}}(T; \xi^\ddagger)$  can be evaluated at the maximum of the free energy barrier at the reaction coordinate  $\xi^\ddagger$ . In practice, it is determined from the centroid potential of the mean force (PMF):<sup>60,63,64</sup>

$$k_{\text{QTST}}(T; \xi^\ddagger) = \frac{4\pi R_\infty^2}{\sqrt{2\pi\mu_R/k_B T}} e^{-(W(\xi^\ddagger) - W(\xi=0))/k_B T}, \quad (7)$$

where  $R_\infty$  is the distance between the two reactants OH and HO<sub>2</sub>, which is required to be sufficiently long (12 Å in this work) to avoid the initial intermolecular interaction.  $W(\xi^\ddagger) - W(\xi=0)$ , the free-energy barrier, is estimated *via* the umbrella integration approach.<sup>70,71</sup>

The second term in eqn (6),  $\kappa(t \rightarrow \infty; \xi^\ddagger)$ , is the long-time limit of a time-dependent ring-polymer transmission coefficient, and provides the dynamic correction that accounts for recrossing at the maximum of the free-energy barrier. This term counterbalances the first factor in eqn (6), ensuring that the final RPMD rate coefficient is not related to the choice of the dividing surface.<sup>68,72</sup>

The RPMD rate theory would approach the classical limit when only one bead is used. At the classical limit, the static and dynamical components are identical to the classical TST rate coefficient and the classical transmission coefficient, respectively.<sup>63</sup> Using more beads can effectively and adequately describe the ZPVE, recrossing and tunneling effects of the systems.<sup>47</sup> The minimal number of beads to account for the quantum effects is estimated according to the following formula:<sup>73</sup>

$$N_{\text{min}} = \hbar \omega_{\text{max}} / k_B T, \quad (8)$$

where  $\omega_{\text{max}}$  denotes the largest vibrational frequency of the stationary points of the reaction system. For R1, this frequency corresponds to the stretching of OH (3749.9 cm<sup>-1</sup>) in the OH radical.

### III. Results and discussion

The PIP-NN PES<sup>42</sup> that has been employed in our previous dynamics and kinetic studies<sup>42,46</sup> was used in the RPMD calculations at the temperatures of 300, 400, 500, 1000 and 1300 K. To accurately and effectively calculate the PMF within the range of the reaction coordinate  $\xi \in (-0.05$  to  $1.1)$ , different widths of windows ( $d\xi$ ) were used for different temperatures and different umbrella force constants ( $k_{\text{ufc}}$ ) were used for different  $\xi$  to get proper overlaps between neighboring windows (see details given in Fig. S1–S5 of the ESI†). As summarized in Table 1, generally, the window interval is set as 0.01, and 2.72 ( $T/K$ ) eV (denoted as  $k_{\text{ufc},0}$ ) is used for  $k_{\text{ufc}}$  at all temperatures. However, special parameters are required for regions particularly near the barrier region where the potential energy varies significantly. At 300 K, 4.08 ( $T/K$ ) eV is used for the product region ( $\xi \in [0.99, 1.1]$ ). In the region near the barrier ( $\xi = 0.98$  and  $0.985$ ), the umbrella force constants are even higher, 5.44 ( $T/K$ ) eV. At 400 K, for  $\xi = 0.99$ ,  $k_{\text{ufc}} = 4.08$  ( $T/K$ ) eV. In the product region, the umbrella force constants are 4.90 and 4.08 ( $T/K$ ) eV at  $\xi \in [1.00, 1.03]$  and  $[1.03, 1.10]$ , respectively. At 500 K, in the region  $\xi \in [0.99, 1.03]$ , larger  $k_{\text{ufc}}$  (1.2–1.8 times  $k_{\text{ufc},0}$ ) values are used. At 1000 K, the umbrella force constant becomes larger, 3.26 ( $T/K$ ) eV for  $\xi = 1.00$ , 1.02 and 4.08 ( $T/K$ ) eV for  $\xi = 1.01$ .

In each window, we ran 60 constrained 100 ps trajectories, and each trajectory was equilibrated by 20 ps under the Andersen thermostat<sup>74</sup> for thermalization. After completing the PMF calculations at each temperature, the next step is to compute the transmission coefficient, the second term in eqn (6). In the beginning, a long mother trajectory (20 ns) starting at the dividing surface is launched with the ring-polymer centroid fixed at the top of the PMF *via* the SHAKE algorithm.<sup>75</sup> The configurations are sampled every 2 ps to serve as the initial positions for 100 child trajectories, which are used to compute the flux-side correlation function. These 100 separate ring polymer trajectories are launched from different initial momenta, which are sampled according to a Boltzmann distribution. These trajectories are run without constraint and thermostat but with different lengths of time: 100, 100, 100, 50, and 50 fs for 300, 400, 500, 1000, and 1300 K, respectively. They are sufficiently long to make the transmission coefficients

reach the plateau values. In the current work, the time step is set as 0.1 fs in all RPMD calculations. The OH radical has a spin-orbital splitting of  $140 \text{ cm}^{-1}$  and the electronic partition function of  $\text{HO}_2$  is 2. Thus, the RPMD rate coefficients are corrected by the following electronic factor:<sup>32</sup>

$$f = \frac{3}{2(2 + 2 \exp(-201.4/T))} \quad (9)$$

Table 1 summarizes the numerical parameters and converged RPMD results for the title reaction: the number of beads ( $N_{\text{beads}}$ ), the maximum of the PMF ( $W(\xi^\ddagger)$ ) and the corresponding reaction coordinate ( $\xi^\ddagger$ ),  $k_{\text{QTST}}$ , the transmission coefficient ( $\kappa$ ), the umbrella force constant ( $k_{\text{ufc}}$ ) and the final RPMD rate coefficients,  $k_{\text{RPMD}}$ .

The 1-bead (classical) and converged (RPMD) PMFs at the temperatures of 300, 400, 500, 1000 and 1300 K are shown in Fig. S6 (ESI†) and Fig. 2, respectively. All PMF curves show similar trends from reactants to products and their transition states are located at around  $\xi = 1.0$ . Firstly, the profiles are nearly flat for  $\xi$  less than about 0.5. The free-energy well (the RC well as shown in Fig. 1) before the transition state, existing only at temperatures of 300, 400, and 500 K, possibly influences the kinetics and dynamics. This well is stabilized mainly by the hydrogen bonding between OH and  $\text{HO}_2$ .<sup>42</sup> At high temperatures (1000 and 1300 K), the well is not shown on the PMF curves. This is because the entropy is decreased from the reactant asymptote to the well. Therefore, the increased temperature can level off the well. Secondly, the free energy barriers, both classical and converged, increase with temperature due to the entropic loss from the reactants to the transition state. The barrier heights of the converged PMFs at 300, 400, 500, 1000, and 1300 K are 0.47, 1.90, 2.99, 7.96, and 9.84 kcal  $\text{mol}^{-1}$ , respectively. The difference is 9.37 kcal  $\text{mol}^{-1}$  between 300 and 1300 K. This is consistent with our previous analysis on the reaction mechanism:<sup>46</sup> at low temperatures, the complex-forming mechanism *via* capture by the RC well dominates, leading to negative temperature-dependent rate coefficients. At higher temperatures, the reaction becomes activated because of the bottleneck formed near the submerged barrier, resulting in Arrhenius behavior. Thirdly, the position of the free energy

**Table 1** Numerical parameters and thermal rate coefficients for the  $\text{OH} + \text{HO}_2 \rightarrow \text{O}_2 + \text{H}_2\text{O}$  reaction. The temperature  $T$  is in K,  $W$  in kcal  $\text{mol}^{-1}$ ,  $k_{\text{ufc}}$  in ( $T/K$ ) eV,  $k_{\text{QTST}}$  and  $k_{\text{RPMD}}$  are in  $\text{cm}^3 \text{ molecule}^{-1} \text{ s}^{-1}$ , and  $\xi^\ddagger$  and  $\kappa$  are dimensionless

$T/K$	300	400	500	1000	1300
$N_{\text{bead}}$	16	16	16	8	8
$\xi^\ddagger$	0.9828	0.9878	0.9895	0.9968	0.9995
$W(\xi^\ddagger)$	0.4700	1.8972	2.9880	7.9559	9.8443
$k_{\text{ufc}}$	2.72 ( $-0.05 \leq \xi \leq 0.97$ )	2.72 ( $-0.05 \leq \xi \leq 0.98$ )	2.72 ( $-0.05 \leq \xi \leq 0.98$ , 1.04 $\leq \xi \leq 1.1$ )	2.72 ( $-0.05 \leq \xi \leq 0.99$ , 1.03 $\leq \xi \leq 1.10$ )	2.72 ( $-0.05 \leq \xi \leq 1.10$ )
	5.44 ( $\xi = 0.98, 0.985$ )	4.08 ( $\xi = 0.99$ )	3.26 ( $\xi = 0.99, 1.03$ )	3.26 ( $\xi = 1.00, 1.02$ )	
	4.08 ( $0.99 \leq \xi \leq 1.10$ )	4.90 ( $1.00 \leq \xi \leq 1.10$ )	4.08 ( $\xi = 1.00, 1.02$ ) 4.90 ( $\xi = 1.01$ )	4.08 ( $\xi = 1.01$ )	
$k_{\text{QTST}}$	$1.76 \times 10^{-9}$	$4.11 \times 10^{-10}$	$2.43 \times 10^{-10}$	$1.27 \times 10^{-10}$	$1.74 \times 10^{-10}$
$\kappa$	0.18900	0.24225	0.28377	0.36766	0.39732
$k_{\text{RPMD}}$	$1.66 \times 10^{-10}$	$4.67 \times 10^{-11}$	$3.11 \times 10^{-11}$	$1.94 \times 10^{-11}$	$2.80 \times 10^{-11}$



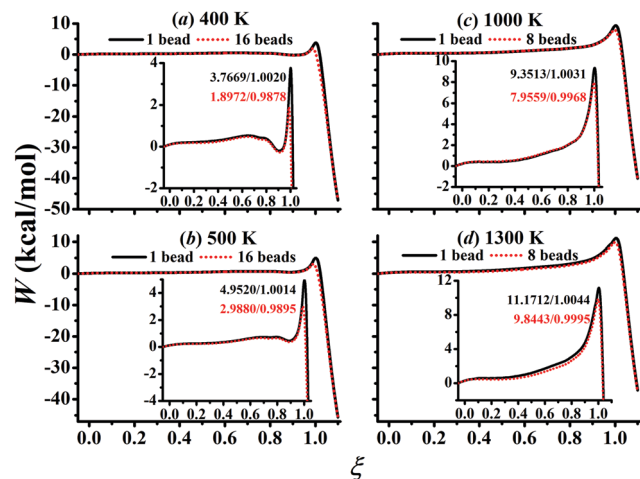


Fig. 2 Potential of mean force (PMF, in kcal mol<sup>-1</sup>, relative to the reactant asymptote OH + HO<sub>2</sub>) along the reaction coordinate at  $T = 400$  (a), 500 (b), 1000 (c), 1300 K (d). The inset shows the detailed characterization of the PMF. The PMF barrier and its position are given in the inset.

barrier shifts towards a larger  $\xi$  as the temperature increases: on the converged PMFs, it increases from  $\xi = 0.9828$  at 300 K to  $\xi = 0.9995$  at 1300 K.

As shown in the insets of Fig. 2 and Fig. S6 (ESI<sup>†</sup>), the converged free energy barrier at each temperature is lower as compared to the classical counterpart, which is an indication of the quantum tunneling effects, particularly at low temperatures. The differences at 300, 400, 500, 1000, and 1300 K are 2.27, 1.87, 1.96, 1.40, and 1.33 kcal mol<sup>-1</sup>, respectively. The difference decreases with the increase in the temperature. The value of  $\xi^\ddagger$  of the converged PMFs is smaller than that of the classical PMFs and the difference diminishes as the temperature goes up. From high to low temperatures, the shifts in the position of the free energy barrier were 0.0005, 0.0030, 0.0105, 0.0122, and 0.0172 for  $T = 1300, 1000, 500, 400$ , and 300 K, respectively. At low temperatures of 300, 400, and 500 K, the significant differences in the free energy barrier height and the peak position between the classical and converged PMFs are apparently due to the strong quantum effect. As the temperature increases, the quantum effect becomes negligible.

Fig. 3 and Fig. S7 (ESI<sup>†</sup>) present the classical and converged RPMD time-dependent transmission coefficients. Roughly speaking, the transmission coefficients have similar trends: the value initially decays rapidly because of the recrossing near the barrier, and then levels off after experiencing a short period of oscillation. These oscillations have little physical meaning and are due to the particular choice of the dividing surface.<sup>76</sup> Like some previous RPMD calculations,<sup>61,76–78</sup> on the one hand, the converged transmission coefficients increase with increasing temperature. On the other hand, the classical transmission coefficients are always larger than the corresponding converged calculations. Besides, the distinction is larger at low temperatures due to the stronger quantum effect. The converged transmission coefficients are very small, all far less than unity: 0.1890, 0.2423, 0.2838, 0.3677 and 0.3973 at 300, 400, 500, 1000,

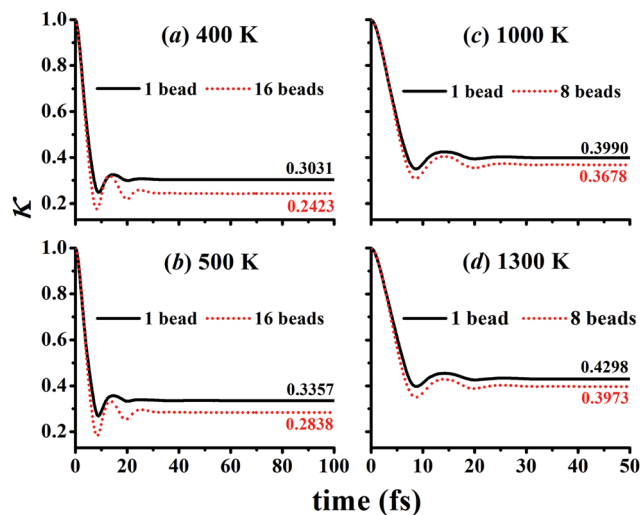


Fig. 3 Transmission coefficients at 400 (a), 500 (b), 1000 (c), 1300 K (d). The asymptotic values of the transmission coefficients are given.

and 1300 K, respectively. The small transmission coefficients indicate that the recrossing is significant even at the PMF barrier. Both the tunneling and recrossing effects are expected to play significant roles for the title reaction since the light hydrogen atom is transferred between the two heavy moieties and the energy barrier is submerged, as shown in Fig. 1. It should be noted that the RPMD transmission coefficients contain contributions from both the classical recrossing and tunneling. The latter, namely the tunneling, has also been included in the PMF calculations with multiple beads. However, it is difficult to separate the tunneling contributions for the PMF and the transmission coefficient within the RPMD framework.<sup>79</sup>

The RPMD and QD rate coefficients are plotted in Fig. 4. The available experimental<sup>1–3,5–28</sup> and theoretical<sup>29,30,32–36,39,42,80</sup> values are also included in this figure for comparison. For clarity, the error bounds are not included. One can see that the available rate coefficients are quite scattered. Experimentally, at around 300 K, the rate coefficients fall within  $2.5 \times 10^{-11}$ – $2 \times 10^{-10}$  cm<sup>3</sup> molecule<sup>-1</sup> s<sup>-1</sup>. Sridharan *et al.* measured the rate coefficients from 252 to 400 K and found a negative temperature dependence.<sup>21</sup> The rate coefficients were less than the experimental observations at 254–382 K by Keyser.<sup>23</sup> The temperature dependences are very similar to each other. No rate coefficients were measured at temperatures within the 420–950 K range. Kappel *et al.* obtained a more reliable  $k_{R1}$  due to the improved detection sensitivity of HO<sub>2</sub> in their work over 950–1250 K and confirmed the non-Arrhenius temperature dependence of  $k_{R1}$ .<sup>26</sup> Hong *et al.* found a weak temperature dependence for  $k_{R1}$  between 1072 and 1283 K based on their high-fidelity measurements.<sup>28</sup> For high temperatures, Srinivasan *et al.* reported  $k_{R1}$  at 1237–1554 K, which ranged from  $3 \times 10^{-11}$  to  $1.25 \times 10^{-10}$  cm<sup>3</sup> molecule<sup>-1</sup> s<sup>-1</sup>.<sup>27</sup> Hippler *et al.* found that there was a rate coefficient minimum near 1250 K according to the measured  $k_{R1}$  at 1150–1600 K.<sup>25</sup> The rate coefficients of the reverse direction of the title reaction were

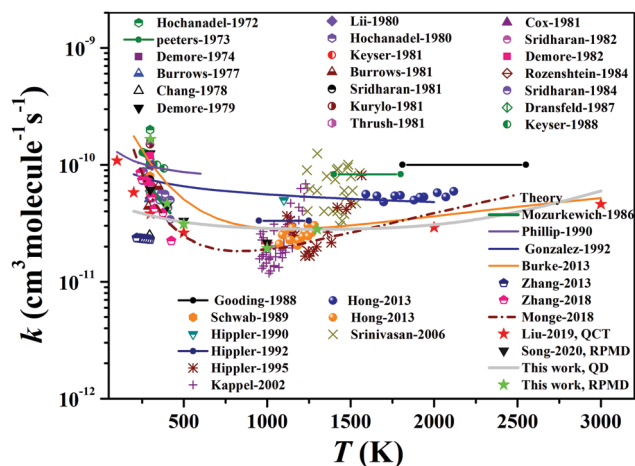


Fig. 4 Comparison of the rate coefficients for the  $\text{OH} + \text{HO}_2 \rightarrow \text{O}_2 + \text{H}_2\text{O}$  reaction.

measured to derive  $k_{\text{R1}}$  at 1600–2200 K by Hong *et al.*, which showed very slight temperature dependence.<sup>5</sup> Goodings *et al.* derived  $k_{\text{R1}}$  at high temperatures 1800–2600 K to be  $(1.0 \pm 0.5) \times 10^{-10} \text{ cm}^3 \text{ molecule}^{-1} \text{ s}^{-1}$ .<sup>3</sup> One can see that the temperature dependence was not consistent among different measurements.

As shown above and discussed by Burke *et al.*,<sup>33</sup> it is difficult to determine a suitable expression for  $k_{\text{R1}}$  due to the lack of consistency in the experimental data and the unusual temperature dependence. Using the multi-scale modeling approach, they incorporated all measured data from the entire temperature range and *ab initio* TST within associated uncertainties. The obtained  $k_{\text{R1}}$ , validated over 200–3000 K, showed a less pronounced temperature dependence with a rate minimum near 1200 K.<sup>33</sup> Therefore, this self-consistent expression of  $k_{\text{R1}}$  can be considered a benchmark for comparison.

For clarity, Fig. 5 compares only the theoretical values. Based on information from only stationary points at CCSD(T)/aug-cc-pVTZ//CCSD/6-311G(d,p), the obtained  $k_{\text{R1}}$  was significantly smaller than

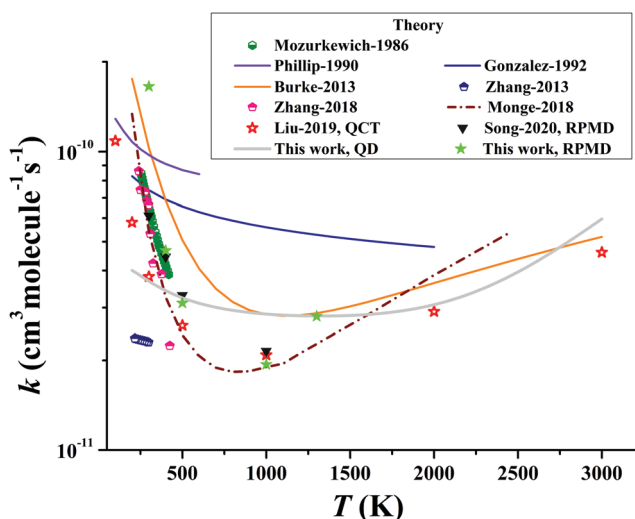


Fig. 5 Comparison of the theoretical rate coefficients for the  $\text{OH} + \text{HO}_2 \rightarrow \text{O}_2 + \text{H}_2\text{O}$  reaction.

most experimental and other theoretical predictions.<sup>34</sup> The  $k_{\text{R1}}$  was then increased to  $2.24\text{--}8.62 \times 10^{-11} \text{ cm}^3 \text{ molecule}^{-1} \text{ s}^{-1}$  over 240–425 K based on electronic information at the level of CCSD(T)/aug-cc-pVTZ//M06-2X/aug-cc-pVTZ.<sup>35</sup> According to the capture model, Phillips obtained  $k_{\text{R1}}$  over 10–600 K but with a slightly negative temperature dependence.<sup>80</sup> Similarly, according to the vibrational/rotational adiabatic capture theory with a dipole-dipole interaction potential between OH and  $\text{HO}_2$ , the  $k_{\text{R1}}$  obtained by Gonzalez *et al.* with information determined at the MP level also showed a slightly negative temperature dependence over 200–2000 K but with a smaller magnitude than those by Phillips.<sup>32</sup> Notably, these two theoretical predictions were overestimated for temperatures of 500 K and above. Besides, the temperature dependences at low temperatures were too weak. Using the microcanonical variational TST at the W3X-L//CCSD=FC/cc-pVTZ level, Monge-Palacios and Sarathy obtained non-Arrhenius rate coefficients with a minimum at 800 K,<sup>36</sup> which agreed well with our previous QCT rate coefficients.<sup>42</sup>

At 400, 500, and 1000 K, the current RPMD rate coefficients are in good agreement with the RPMD results computed by Song *et al.*<sup>39</sup> and are both close to the QCT calculated ones due to the slight quantum effect at these temperatures. Compared to those by Burke *et al.*, the RPMD results in the current work and by Song *et al.*, and the QCT results, are significantly lower in the intermediate temperatures of 400–1200 K. At 300 K, the QCT calculated result was smaller than that by Monge-Palacios and Sarathy<sup>36</sup> and by Song *et al.* using RPMD,<sup>39</sup> with the latter two being consistent with each other. Interestingly, the current RPMD result at 300 K is much higher than that by Song *et al.* using the same RPMD calculation but on a different PES. Considering that the same RPMD method was employed in the rate constant calculations, the large difference at 300 K is most likely caused by the subtle difference along the minimum energy path. However, our RPMD result is in better agreement with that suggested by Burke *et al.*<sup>33</sup> Since no details on the RPMD calculation by Song *et al.* were available, further comparison and discussion cannot be made. Special treatments were adopted in our *ab initio* calculations to obtain reliable and smooth potential energy curves for the PIP-NN PES.<sup>46</sup> Thus, the PIP-NN PES is expected to provide a better description for the PES of the title system. For RPMD calculations on the PIP-NN PES, the ratios for many beads: 1 bead rate coefficients are 31.7, 8.9, 2.77, 1.88, and 1.53 at 300, 400, 500, 1000, 1300 K, respectively, an indicator of the strong quantum effect, particularly at low temperatures.

The calculated results by the reduced QD model were flat at temperatures up to 2000 K, and increased notably at high temperatures. At intermediate temperatures, the QD results agreed well with those by Burke *et al.*<sup>33</sup> However, at a low temperature of around 300 K, the QD results were significantly smaller. It should be pointed out that the current QD rate coefficients were obtained from the reactant ground ro-vibrational states. In our earlier studies,<sup>46</sup> the excitation in the H–OO stretch (the reactant  $\text{HO}_2$ ) showed a dramatic enhancement effect at low collision energies because this mode involves the motion of the transferring H. The enhancement

factor is as large as 4 at  $E_c = 2.5 \text{ kcal mol}^{-1}$ . The vibrational excitation of the reactant OH promotes the reactivity as well at low collision energies, with an enhancement factor larger than 2 at  $E_c = 1 \text{ kcal mol}^{-1}$ . The excitations in the reactant rotations can help guide the reactants towards the RC well at low temperatures, thus enhancing the reactivity. The thermal population of these reactant modes is expected to enhance the reactivity at low temperatures as compared with that from the ground ro-vibrational state reactants. At high temperatures, the QD rate constants agree well with the QCT results, implying that the quantum effect is negligible.

## IV. Conclusions

In this work, we employed the RPMD and reduced-dimensional QD approaches to revisit the prototypical radical-radical reaction  $\text{OH} + \text{HO}_2 \rightarrow \text{H}_2\text{O} + \text{O}_2$  on our previously fitted global full-dimensional PIP-NN PES. The quantum effects were examined by comparing the current rate coefficients with earlier QCT results. The QD rate coefficients agree well with the QCT calculations at high temperatures above 2000 K and at low temperature 300 K, while they are visibly larger than the QCT ones at moderate temperatures between 300 K and 2000 K. The RPMD coefficients are in good agreement with the QCT values at temperatures in between 300 K and 1000 K, and become significantly larger at low temperatures, indicating the non-negligible quantum effects at low temperatures. The discrepancy between the QD and RPMD rate coefficients is most likely caused by the neglect of the effect from the reactant excited ro-vibrational states in the QD calculations. Besides, the small transmission coefficients in RPMD calculations indicate that the recrossing of this reaction is exceedingly significant, especially at low temperatures.

## Conflicts of interest

There are no conflicts of interest to declare.

## Acknowledgements

This work was financially supported by National Natural Science Foundation of China (21973009 to J. L., 21973109 to H. S.) and Chongqing Municipal Natural Science Foundation (grant no. cstc2019jcyj-msxmX0087 to J. L.). Y. L. thanks the support from the China Scholarship Council (CSC). J. L. acknowledges the Alexander von Humboldt Foundation for a Humboldt Fellowship for Experienced Researchers.

## References

- 1 J. P. Burrows, G. W. Harris and B. A. Thrush, *Nature*, 1977, **267**, 233–234.
- 2 J. Peeters and G. Mahnen, *Symp. Combust.*, 1973, **14**, 133–146.
- 3 J. M. Goodings and A. N. Hayhurst, *J. Chem. Soc., Faraday Trans. 2*, 1988, **84**, 745–762.
- 4 E. L. Petersen, D. F. Davidson and R. K. Hanson, *Combust. Flame*, 1999, **117**, 272–290.
- 5 Z. Hong, S. S. Vasu, D. F. Davidson and R. K. Hanson, *J. Phys. Chem. A*, 2010, **114**, 5520–5525.
- 6 W. B. DeMore, *J. Phys. Chem.*, 1982, **86**, 121–126.
- 7 C. J. Hochenadel, J. A. Ghormley and P. J. Ogren, *J. Chem. Phys.*, 1972, **56**, 4426–4432.
- 8 W. B. DeMore and E. Tschuikow-Roux, *J. Phys. Chem.*, 1974, **78**, 1447–1451.
- 9 J. S. Chang and F. Kaufman, *J. Phys. Chem.*, 1978, **82**, 1683–1687.
- 10 W. B. DeMore, *J. Phys. Chem.*, 1979, **83**, 1113–1118.
- 11 C. J. Hochenadel, T. J. Sworski and P. J. Ogren, *J. Phys. Chem.*, 1980, **84**, 3274–3277.
- 12 R.-R. Lii, R. A. Gorse, M. C. Sauer and S. Gordon, *J. Phys. Chem.*, 1980, **84**, 819–821.
- 13 J. P. Burrows, R. A. Cox and R. G. Derwent, *J. Photochem.*, 1981, **16**, 147–168.
- 14 R. A. Cox, J. P. Burrows and T. J. Wallington, *Chem. Phys. Lett.*, 1981, **84**, 217–221.
- 15 L. F. Keyser, *J. Phys. Chem.*, 1981, **85**, 3667–3673.
- 16 M. J. Kurylo, O. Klais and A. H. Laufer, *J. Phys. Chem.*, 1981, **85**, 3674–3678.
- 17 U. C. Sridharan, L. X. Qiu and F. Kaufman, *J. Phys. Chem.*, 1981, **85**, 3361–3363.
- 18 B. A. Thrush and J. P. T. Wilkinson, *Chem. Phys. Lett.*, 1981, **81**, 1–3.
- 19 U. C. Sridharan, L. X. Qiu and F. Kaufman, *J. Phys. Chem.*, 1982, **86**, 4569–4574.
- 20 V. B. Rozenshtein, Y. M. Gershenzon, S. D. Il'in and O. P. Kishkovitch, *Chem. Phys. Lett.*, 1984, **112**, 473–478.
- 21 U. C. Sridharan, L. X. Qiu and F. Kaufman, *J. Phys. Chem.*, 1984, **88**, 1281–1282.
- 22 P. Dransfeld and H. G. Wagner, *Z. Naturforsch., A: Phys. Sci.*, 1987, **42**, 471.
- 23 L. F. Keyser, *J. Phys. Chem.*, 1988, **92**, 1193–1200.
- 24 J. J. Schwab, W. H. Brune and J. G. Anderson, *J. Phys. Chem.*, 1989, **93**, 1030–1035.
- 25 H. Hippler, H. Neunaber and J. Troe, *J. Chem. Phys.*, 1995, **103**, 3510–3516.
- 26 C. Kappel, K. Luther and J. Troe, *Phys. Chem. Chem. Phys.*, 2002, **4**, 4392–4398.
- 27 N. K. Srinivasan, M.-C. Su, J. W. Sutherland, J. V. Michael and B. Ruscic, *J. Phys. Chem. A*, 2006, **110**, 6602–6607.
- 28 Z. Hong, K.-Y. Lam, R. Sur, S. Wang, D. F. Davidson and R. K. Hanson, *Proc. Combust. Inst.*, 2013, **34**, 565–571.
- 29 M. Mozurkewich, *J. Phys. Chem.*, 1986, **90**, 2216–2221.
- 30 D. W. Toohey and J. G. Anderson, *J. Phys. Chem.*, 1989, **93**, 1049–1058.
- 31 C. Gonzalez, J. Theisen, L. Zhu, H. B. Schlegel, W. L. Hase and E. W. Kaiser, *J. Phys. Chem.*, 1991, **95**, 6784–6792.
- 32 C. Gonzalez, J. Theisen, H. B. Schlegel, W. L. Hase and E. W. Kaiser, *J. Phys. Chem.*, 1992, **96**, 1767–1774.
- 33 M. P. Burke, S. J. Klippenstein and L. B. Harding, *Proc. Combust. Inst.*, 2013, **34**, 547–555.
- 34 T. Zhang, W. Wang, C. Li, Y. Du and J. Lü, *RSC Adv.*, 2013, **3**, 7381–7391.

- 35 T. Zhang, X. Lan, Z. Qiao, R. Wang, X. Yu, Q. Xu, Z. Wang, L. Jin and Z. Wang, *Phys. Chem. Chem. Phys.*, 2018, **20**, 8152–8165.
- 36 M. Monge-Palacios and S. M. Sarathy, *Phys. Chem. Chem. Phys.*, 2018, **20**, 4478–4489.
- 37 J. Cui and R. V. Krems, *J. Phys. B: At., Mol. Opt. Phys.*, 2016, **49**, 224001.
- 38 A. Kamath, R. A. Vargas-Hernández, R. V. Krems, T. Carrington Jr. and S. Manzhos, *J. Chem. Phys.*, 2018, **148**, 241702.
- 39 Q. Song, Q. Zhang and Q. Meng, *J. Chem. Phys.*, 2020, **152**, 134309.
- 40 S. Habershon, D. E. Manolopoulos, T. E. Markland and T. F. Miller III, *Annu. Rev. Phys. Chem.*, 2013, **64**, 387–413.
- 41 E. Uteva, R. S. Graham, R. D. Wilkinson and R. J. Wheatley, *J. Chem. Phys.*, 2018, **149**, 174114.
- 42 Y. Liu, M. Bai, H. Song, D. Xie and J. Li, *Phys. Chem. Chem. Phys.*, 2019, **21**, 12667–12675.
- 43 B. Jiang and H. Guo, *J. Chem. Phys.*, 2013, **139**, 054112.
- 44 J. Li, B. Jiang and H. Guo, *J. Chem. Phys.*, 2013, **139**, 204103.
- 45 B. Jiang, J. Li and H. Guo, *Int. Rev. Phys. Chem.*, 2016, **35**, 479–506.
- 46 Y. Liu, H. Song, D. Xie, J. Li and H. Guo, *J. Am. Chem. Soc.*, 2020, **142**, 3331–3335.
- 47 Y. V. Suleimanov, F. J. Aoiz and H. Guo, *J. Phys. Chem. A*, 2016, **120**, 8488–8502.
- 48 J. F. Castillo and Y. V. Suleimanov, *Phys. Chem. Chem. Phys.*, 2017, **19**, 29170–29176.
- 49 S. Bhowmick, D. Bossion, Y. Scribano and Y. V. Suleimanov, *Phys. Chem. Chem. Phys.*, 2018, **20**, 26752–26763.
- 50 Y. V. Suleimanov, A. Aguado, S. Gómez-Carrasco and O. Roncero, *J. Phys. Chem. Lett.*, 2018, **9**, 2133–2137.
- 51 T. González-Lezana, D. Bossion, Y. Scribano, S. Bhowmick and Y. V. Suleimanov, *J. Phys. Chem. A*, 2019, **123**, 10480–10489.
- 52 J. Z. H. Zhang, *Theory and Application of Quantum Molecular Dynamics*, World Scientific, Singapore, 1999.
- 53 H. Song, J. Li, M. Yang, Y. Lu and H. Guo, *Phys. Chem. Chem. Phys.*, 2014, **16**, 17770–17776.
- 54 D. H. Zhang and J. Z. H. Zhang, *J. Chem. Phys.*, 1993, **99**, 5615.
- 55 J. A. Flect Jr., J. R. Morris and M. D. Feit, *Appl. Phys.*, 1976, **10**, 129.
- 56 R. T. Pack, *J. Chem. Phys.*, 1974, **60**, 633–639.
- 57 P. McGuire and D. J. Kouri, *J. Chem. Phys.*, 1974, **60**, 2488–2499.
- 58 D. Neuhauser and M. Baer, *J. Chem. Phys.*, 1989, **90**, 4351.
- 59 W. H. Miller, S. D. Schwartz and J. W. Tromp, *J. Chem. Phys.*, 1983, **79**, 4889–4899.
- 60 Y. V. Suleimanov, J. W. Allen and W. H. Green, *Comput. Phys. Commun.*, 2013, **184**, 833–840.
- 61 Y. V. Suleimanov, R. P. de Tudela, P. G. Jambrina, J. F. Castillo, V. Sáez-Rábanos, D. E. Manolopoulos and F. J. Aoiz, *Phys. Chem. Chem. Phys.*, 2013, **15**, 3655–3665.
- 62 D. Chandler, *J. Chem. Phys.*, 1978, **68**, 2959–2970.
- 63 R. Collepardo-Guevara, Y. V. Suleimanov and D. E. Manolopoulos, *J. Chem. Phys.*, 2009, **130**, 174713.
- 64 Y. V. Suleimanov, R. Collepardo-Guevara and D. E. Manolopoulos, *J. Chem. Phys.*, 2011, **134**, 044131.
- 65 M. J. Gillan, *Phys. Rev. Lett.*, 1987, **58**, 563–566.
- 66 M. J. Gillan, *J. Phys. C: Solid State Phys.*, 1987, **20**, 3621–3641.
- 67 G. A. Voth, D. Chandler and W. H. Miller, *J. Chem. Phys.*, 1989, **91**, 7749–7760.
- 68 I. R. Craig and D. E. Manolopoulos, *J. Chem. Phys.*, 2005, **123**, 034102.
- 69 R. Collepardo-Guevara, I. R. Craig and D. E. Manolopoulos, *J. Chem. Phys.*, 2008, **128**, 144502.
- 70 J. Kästner and W. Thiel, *J. Chem. Phys.*, 2005, **123**, 144104.
- 71 J. Kästner and W. Thiel, *J. Chem. Phys.*, 2006, **124**, 234106.
- 72 Y. V. Suleimanov, *J. Phys. Chem. C*, 2012, **116**, 11141–11153.
- 73 T. E. Markland and D. E. Manolopoulos, *J. Chem. Phys.*, 2008, **129**, 024105.
- 74 H. C. Andersen, *J. Chem. Phys.*, 1980, **72**, 2384–2393.
- 75 J.-P. Ryckaert, G. Ciccotti and H. J. C. Berendsen, *J. Comput. Phys.*, 1977, **23**, 327–341.
- 76 H. Wang, J. Fang, H. Yang, J. Song and Y. Li, *Chem. Phys. Lett.*, 2019, **730**, 227–233.
- 77 D. Lu, Y. Zhang and J. Li, *Chem. Phys. Lett.*, 2018, **694**, 93–101.
- 78 M. Bai, D. Lu, Y. Li and J. Li, *Phys. Chem. Chem. Phys.*, 2016, **18**, 32031–32041.
- 79 J. Zuo, Y. Li, H. Guo and D. Xie, *J. Phys. Chem. A*, 2016, **120**, 3433–3440.
- 80 L. F. Phillips, *J. Phys. Chem.*, 1990, **94**, 7482–7487.